Sun *et al. Biochar* (2026) 8:12
https://doi.org/10.1007/s42773-025-00526-3

Biochar

ORIGINAL RESEARCH Open Access

Co-engineering biochar and artificial humic substances: advancing photoreduction performance through structure design

Liming Sun[1,2], Minghao Shen[1], Chao Jia[1], Fengbo Yu[1,2], Shicheng Zhang[1,3*] and Xiangdong Zhu[1,2*]

Abstract

Engineered biochar with enhanced photochemical properties holds great potential for environmental remediation. However, natural humic substances, crucial players in environmental redox processes, are structurally complex and slow-forming, hindering mechanistic insights and practical applications. Here, we propose a co-engineering strategy that combines biochar with artificial humic substances synthesized from pine sawdust via controlled hydrothermal humification (180–340 °C). Modulating the hydrothermal temperature can yield artificial humic substances with diverse degradation degrees of lignin, yielding tailored phenolic architectures and electron-donating capacities (EDC). Using Ag^+ photoreduction as a model reaction, we demonstrate that artificial humic substances produced at 340 °C exhibit optimal phenol content and the strongest reducing capacity (19.2-fold greater than that of substances synthesized at 180 °C). Notably, higher molecular weight fractions (> 5 kDa) of artificial humic substances were found to dominate Ag^+ photoreduction due to their enriched phenolic content and superior EDC. Mechanistic investigations reveal that photo-excited phenolic groups generate superoxide radical ($O_2^{\bullet-}$), initiating Ag^+ reduction via a ligand-to-metal charge transfer (LMCT) pathway. Moreover, we discovered a previously overlooked phenomenon: hydrochar undergoes photo-induced dissolution, further enhancing photoreduction. This work provides new insights into the temperature-dependent lignin transformation into redox-active artificial humic substances and highlights the dynamic photochemical behavior of engineered biochar (hydrochar) under solar irradiation.

Highlights

- Modulating hydrothermal temperature yields varied lignin degradation progress.
- 340 °C-synthesized artificial humic substances showed 19-fold higher Ag^+ reduction than 180 °C-synthesized samples.
- O_2•− generation by photo-excited phenolic groups drives silver reduction, followed by a ligand-to-metal charge transfer process.
- Sunlight exposure triggers dynamic hydrochar transformation, revealing new pathways for photoreduction processes.

*Correspondence:
Shicheng Zhang
zhangsc@fudan.edu.cn
Xiangdong Zhu
xdzhu@issas.ac.cn; zxdjewett@fudan.edu.cn
Full list of author information is available at the end of the article

Keywords Engineered biochar, Hydrothermal humification, Artificial humic substance, Photoreduction, Electron-donating capacities, Dynamic photochemical behavior

Graphical Abstract

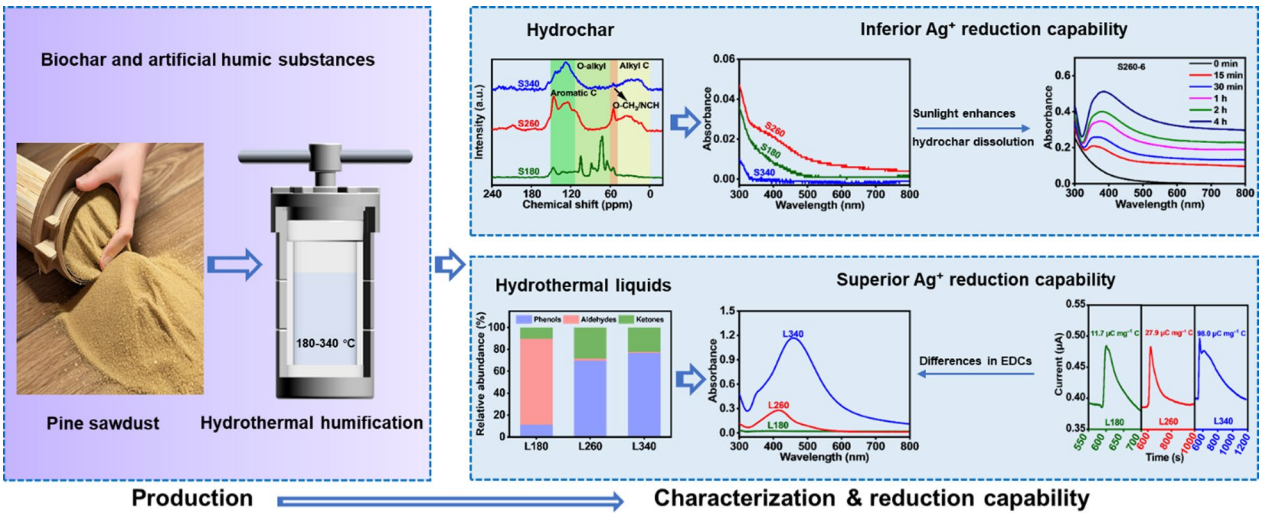

1 Introduction

Engineered biochar has emerged as a promising material for environmental applications due to its excellent sorptive and catalytic properties (Khan et al. 2023; Yameen et al. 2024). However, its photochemical behavior, especially under natural sunlight, remains insufficiently understood. Meanwhile, natural humic substances are known to mediate redox reactions in aquatic and soil systems (Peng et al. 2022), yet their structural heterogeneity and slow natural formation via plant residue decomposition (Tang et al. 2021; Yang et al. 2021) limit mechanistic studies and practical applications (Yang et al. 2021; Zingaretti et al. 2018).

To overcome these challenges, artificial humic substances synthesized via hydrothermal humification offer a tunable and rapid alternative (Yang et al. 2019). Using plant-derived biomass, this process mimics the natural humification of lignin-rich matter but provides precise control over the molecular structure (Xu et al. 2023; Yang et al. 2019). Unlike dissolved black carbon (DBC) derived from biochar, which lacks structural flexibility (Li et al. 2020; Liu et al. 2021), hydrothermally produced artificial humic substances enable the adjustment of phenolic density and redox potential. In this study, we systematically explore how hydrothermal temperature modulates the phenolic architecture and electron-donating capacity of artificial humic substances, as well as the resulting effects on their photoreduction performance.

Biochar's photochemical activity heavily relies on its aromaticity and surface functional groups (Khan et al. 2023). However, existing studies predominantly focus on dissolved organic fractions, overlooking the dynamic photochemical roles of undissolved biochar. To address this gap, we explore a previously overlooked phenomenon—the photo-induced dissolution of hydrochar—revealing a novel pathway that enhances biochar's function as a photochemical mediator. Compared to cellulose/hemicellulose (Chen et al. 2020), the recalcitrant nature of lignin (Okolie et al. 2021) allows precise tuning of phenolic architectures during hydrothermal treatment, directly governing the reducibility of the resultant products (Hao et al. 2018; Wang et al. 2022).

Ag^+ photoreduction serves as an ideal model reaction for evaluating the photochemical reduction performance of engineered biochar and artificial humic substances, providing both spectroscopic evidence (via silver nanoparticle formation) and environmental relevance. Silver nanoparticles (AgNPs) are widely utilized for their remarkable antimicrobial properties (Guo et al. 2018; Rtimi et al. 2019); however, concerns regarding their potential environmental risks persist (Dong et al. 2019; Yu et al. 2018). Numerous studies have focused on Ag^+ reduction by dissolved humic substances (Dong et al. 2020; Hou et al. 2013; Jain and Mehata 2017; Zou et al. 2015), but the contribution of undissolved fractions remains unclear (Huang et al. 2019; Nie et al. 2019),

particularly regarding aromatic versus aliphatic component interactions (Akaighe et al. 2011; Nie et al. 2019).

This study presents an innovative co-engineering strategy combining biochar with artificial humic substances via regulated hydrothermal humification. We elucidate the mechanisms underlying Ag^+ photoreduction mediated by artificial humic substances with varying lignin degradation degrees and the molecular weights (MW) under simulated sunlight. The photoreduction mechanisms of AgNP formation mediated by artificial humic substances were analyzed in detail. Crucially, we reveal that hydrochar's photo-induced dissolution under sunlight provides novel insights into the undissolved biochar's previously overlooked role in environmental redox processes (Huang et al. 2019).

This co-engineering strategy not only accelerates the humification process compared to natural pathways but also provides a tunable platform to investigate the redox behavior of trace metals (e.g., Ag^+) and organic pollutants. Collectively, these insights advance the design of solar-responsive remediation materials and deepen our understanding of metal geochemical cycling in sunlit environments.

2 Materials and methods

2.1 Preparation of hydrochar and artificial humic substances

Artificial humic substances were prepared via one-step hydrothermal liquefaction (HTL) using waste biomass as a precursor (Yang et al. 2019). In a 500 mL autoclave, pine sawdust and ultrapure water were combined at a ratio of 1:10 and subjected to hydrothermal humification to simulate lignin degradation. For the experiments conducted at 180 °C and 260 °C, 30 g of pine sawdust was mixed with 300 mL of ultrapure water. For the experiment at 340 °C, 10 g of pine sawdust was mixed with 100 mL of ultrapure water. Each reaction was sustained for 2 h, after which the autoclave was cooled to room temperature using tap water. The obtained solid and liquid phase samples were separated and recovered via filtration and denoted as S-X and L-X, respectively, with *S* representing the hydrochar, *L* representing the dissolved artificial humic substances (hydrothermal liquid), and *X* representing the HTL temperature (180–340 °C). Furthermore, to study the impact of long-term irradiation on the dissolution of hydrochar, S260 was selected as an example after 0–6 weeks of irradiation (see SI for details).

2.2 Dissolved artificial humic substances fractionation

To investigate the effect of dissolved artificial humic substances with different MW on the photoreduction of Ag^+ to AgNPs, a part of pristine L340 (< 0.22 μm) was fractionated by a series of Ultracel regenerated cellulose ultrafiltration membranes with nominal MW cut-offs of 50, 5, and 1 kDa (Amicon Bioseparations, Millipore). The filtrates were collected and denoted as MW-fractionated L340 (< 50 kDa, < 5 kDa, < 1 kDa M_f-L340).

2.3 Formation of AgNPs under simulated sunlight

The AgNPs were formed by mixing $AgNO_3$ with a representative dissolved artificial humic substance (L340) at room temperature under simulated sunlight irradiation. The L340 concentration varied from 17.8 to 71.3 mg C L^{-1}, the $AgNO_3$ concentration varied from 0.1 to 1×10^{-3} mol L^{-1}, and the S340 concentration was fixed at 100 mg L^{-1}. Photoreduction experiments were performed using a solar simulator (PLS-SXE300DUV, Beijing Perfect Light Co., Ltd., China) equipped with a 300 W xenon lamp (light source: 320–780 nm) without light filters at 500 mW cm^{-2}. The mixed suspension (200 mL) was added to a top-illuminated photoreactor and covered with a quartz water jacket glass slide. During simulated sunlight irradiation, the reaction temperature was maintained at room temperature by passing tap water into the reactor. For kinetic testing, samples were collected through a syringe at specific time intervals for further analysis. $AgNO_3$ or artificial humic substances were used as controls and no buffer solution was added to the reaction system. To investigate the effect of dissolved oxygen on the photoreduction of Ag^+, the mixed solution was continuously purged with high-purity nitrogen or air during the reaction. To evaluate the role of $O_2^{\bullet-}$ in the photoreduction of Ag^+, superoxide dismutase (SOD, 3 kU mL^{-1}) was added before the reaction.

2.4 Characterizations of artificial humic substances

The C, H, N, and O contents of the hydrochar were measured using an elemental analyzer (Vario EL III). The chemical functional groups of the undissolved artificial humic substances were analyzed using solid-state ^{13}C nuclear magnetic resonance (Bruker 400 M). The chemical composition of the dissolved artificial humic substances was determined using gas chromatography-mass spectrometry (GC–MS, Thermo Focus DSQ), and the total phenolic content of L340 was determined using the Folin-Ciocalteu method (Wang et al. 2011) (see SI for details). Fourier transform ion cyclotron resonance mass spectrometry (FT-ICR MS, Bruker) was employed to analyze the molecular composition of dissolved artificial humic substances (Qian et al. 2018) (see SI for details). Mediated electrochemical oxidation (MEO) was utilized to quantitatively determine the EDC of L340 at a constant potential, according to a previous study (Aeschbacher et al. 2010) (see SI for details). The chemical differences between the L340 fractions were assessed using a fluorometer (Aqualog, Horiba-Jobin Yvon, USA).

Excitation-emission matrix (EEM) spectra were measured at the excitation wavelength of 200–500 nm in 3 nm intervals and emission wavelength of 200–500 nm in 2 nm intervals for each excitation wavelength. The total organic carbon (TOC) of dissolved artificial humic substances was determined using a TOC analyzer (TOC-L CPH, Shimadzu, Japan).

2.5 Characterization of AgNPs

At each time point, the UV–vis spectra of AgNPs from 300 to 800 nm were recorded using a double-beam ultraviolet–visible spectrophotometer (TU-1901, Beijing Purkinje General Instrument Co., Ltd., China). The mass concentration of AgNPs was measured using ultrafiltration coupled with inductively coupled plasma mass spectrometry (ICP-OES, Perkin Elmer Optima-8000). Before ICP analysis, the AgNP suspensions were transferred to 3 kDa ultrafiltration centrifuge tubes (Amicon Ultra-15, 3 kDa, Millipore) and centrifuged at 5000 g for 40 min (Li et al. 2018). AgNP concentration was calculated by subtracting the Ag^+ concentration from the total Ag concentration. The residuals on the filters were rinsed with deionized water and freeze-dried using a SCIENTZ-10N freeze dryer (Ningbo Scientz Biotechnology Co., Ltd., China) for X-ray photoelectron spectroscopy (XPS) and X-ray diffraction (XRD) characterizations. The valence state of Ag was determined using XPS (PHI 5000C&PHI5300, USA). The morphology of AgNPs was observed using a high-resolution transmission electron microscope (HR-TEM, Tecnai G^2 F20 S-Twin, FEI, USA) equipped with energy dispersive X-ray spectrometry (EDS) and selected area electron diffraction (SAED) at an acceleration voltage of 200 kV. The TEM specimens were prepared by slowly drop-drying the solution on a 300-mesh ultrathin carbon-coated copper grid.

3 Results and discussion

3.1 Characteristics of hydrochar and artificial humic substances

To elucidate the reductive properties of hydrochar and artificial humic substances, the properties of hydrochar were first investigated. The S340 samples contained more carbon (76.0%) and less oxygen (18.0%) than the sawdust, S180, and S260 samples, suggesting that hydrothermal liquefaction at high temperatures accelerated lignin degradation (Table S1). Furthermore, the hydrochar obtained at diverse hydrothermal temperatures mainly followed a dehydroxylation trend, as confirmed by the Van Krevelen diagrams (Fig. 1a). The aromaticity of the hydrochar followed the order S340 > S260 > S180, indicating that the biomass feedstock (sawdust) experienced more intense dehydration and condensation reactions at higher hydrothermal temperatures (Fig. 1b and Table S2). The carbon conversion rate of the diverse artificial humic substances decreased with an increase in hydrothermal temperature (Figs. S1-2, Fig. 1c, and Table S1).

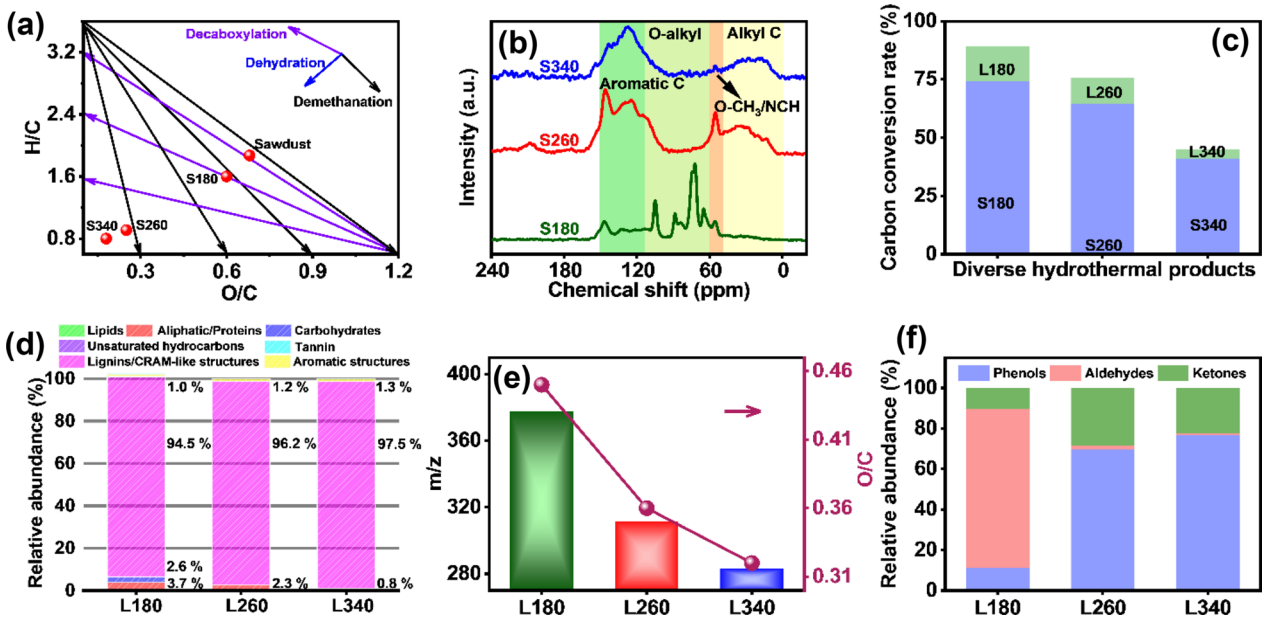

Fig. 1 Characteristics of hydrochar and artificial humic substances. **a** Evolution of H/C and O/C atomic ratios in the Van Krevelen diagram. **b** Solid-state ^{13}C NMR spectra of hydrochar. **c** Carbon conversion rates of different hydrochars and artificial humic substances. **d** Contributions of major CHO subcategories in dissolved artificial humic substances. **e** The m/z and O/C ratio of dissolved artificial humic substances. **f** GC–MS analysis of dissolved artificial humic substances (DOC = 35.6 mg C L^{-1})

Moreover, FT-ICR MS was used to characterize the molecular composition of the dissolved artificial humic substances (hydrothermal liquid). The molecular compositions of artificial humic substances are presented in typical Van Krevelen diagrams (Fig. S3). The three artificial humic substances were mainly distributed in the lignins/ carboxylic-rich alicyclic molecule–like (CRAM) structural region (Fig. 1d). The Van Krevelen diagrams revealed that the hydrothermal temperature facilitated the transformation of compounds from lignin/CRAM structures to aromatic structures, as indicated by the decrease in H/C values (Fig. S4). Additionally, low-polarity and low-molecular-weight compounds were readily formed at elevated temperatures, as demonstrated by the decrease in m/z and O/C ratios from 377.8 to 282.9 and from 0.45 to 0.32, respectively (Fig. 1e). Consequently, relatively abundant compounds with more than 7 oxygen atoms and m/z > 400 were distinctly transformed into substances with lower molecular weight and lower oxygen content (Figs. S5-S6). This transformation is attributed to the gradual depolymerization and dehydration of lignocellulose, resulting in bond breakages and oxygen separation with increasing hydrothermal temperature.

GC–MS further demonstrated that the concentrations of low-molecular-weight compounds, specifically phenols and ketones, typical redox-active components, were notably elevated in artificial humic substances produced at 260 and 340 °C (Fig. 1f and Table S3). The total phenolic concentration in these substances followed the order L340 > L260 > L180 (Fig. S7), as determined using the modified Folin – Ciocalteu method (Wang et al. 2011). The EEM results confirmed that substances exhibiting peaks at 239/330 and 287/326 nm (excitation/emission) were associated with phenol-like compounds resulting from lignin depolymerization (Fig. S8) (Hao et al. 2018; Yu et al. 2022). The fluorescence intensity notably increased at higher hydrothermal temperatures, indicating a corresponding increase in the concentration of these compounds. Consequently, differences in the phenol content may account for variations in the reduction performance of artificial humic substances.

3.2 Photoreduction of Ag^+ to AgNPs by artificial humic substances

The phenolic moieties of humic substances can mediate the conversion of minerals or pollutants into electron-donating groups (Lv et al. 2018; Walpen et al. 2018; Yang et al. 2023). The EDCs were measured to confirm the reductive capacities of various artificial humic substances. The EDCs of artificial humic substances followed the order L340 > L260 > L180 (Fig. 2a), indicating that artificial humic substances with higher phenol content possessed stronger reductive properties. Herein, taking the trace metal Ag as a probe, we evaluated the reductive capacity of artificial humic substances under simulated sunlight. Compared to the L180 and L260 samples, the L340 sample significantly accelerated Ag^+ reduction efficiency under simulated sunlight by more than 19.2 or 4.7-fold, respectively (Fig. 2b,c). The rate of photochemically induced growth of AgNPs followed the order L340 > L260 > L180, which was consistent with the trend of phenol content in the samples. Moreover, TEM images confirmed that dissolved artificial humic substances prepared at high temperatures can significantly promote the growth of AgNPs under simulated sunlight (Fig. S9). As expected, hydrochar prepared at the three hydrothermal temperatures did not lead to the formation of the characteristic peak of AgNPs under simulated sunlight (Fig. 2d).

Based on these comparative results, L340 was selected as the model reducing agent for detailed investigation of the Ag^+ photoreduction mechanism. Using optimized conditions (1 mmol L^{-1} $AgNO_3$ and 59.7 mg C L^{-1} DOC of L340 (< 50 kDa)), we systematically characterized the photoreduction process under simulated sunlight. The relatively colorless solution turned light yellow upon light exposure, and the color deepened as irradiation continued (Fig. S10). Moreover, the absorbance increased with longer irradiation time, and the characteristic peak (~ 400 nm) of AgNPs gradually shifted to longer wavelengths (Fig. S10), indicating that the formation rate of AgNPs accelerated. Control samples without light exposure or containing only $AgNO_3$ showed no obvious characteristic peak of AgNPs, indicating that the formation of AgNPs required light exposure and artificial humic substances (Fig. S11). With prolonged irradiation, the morphology of AgNPs in the presence of L340 changed from an initial spherical or quasi-spherical shape to triangular or other polygonal shapes, and eventually aggregated and eventually formed rod-like or larger nanoclusters (Fig. S12). The concentration of AgNPs increased from 27.9 mg L^{-1} after 15 min to 47.8 mg L^{-1} after 4 h of irradiation (Fig. S13). Furthermore, the SAED pattern of AgNPs formed in the 4 h sample shows four face-centered cubic planes: (111), (200), (220), and (311) planes of elemental Ag (Fig. S14a). EDS further confirmed the presence of metallic Ag (Fig. S14b). In the XRD analysis, a prominent diffraction peak emerged at 37.9° in the lyophilized sample, corresponding to the (111) crystal plane of metallic Ag (Fig. S15). The presence of elemental Ag species was further verified using XPS analysis. As depicted in Fig. S16, the Ag $3d_{5/2}$ and Ag $3d_{3/2}$ signals appeared at 367.9 eV and 373.9 eV, indicating the presence of metallic Ag (Huang et al. 2019). In summary, the qualitative or quantitative characterization methods of UV–vis, TEM-EDS, XRD, XPS, and ICP-OES proved that

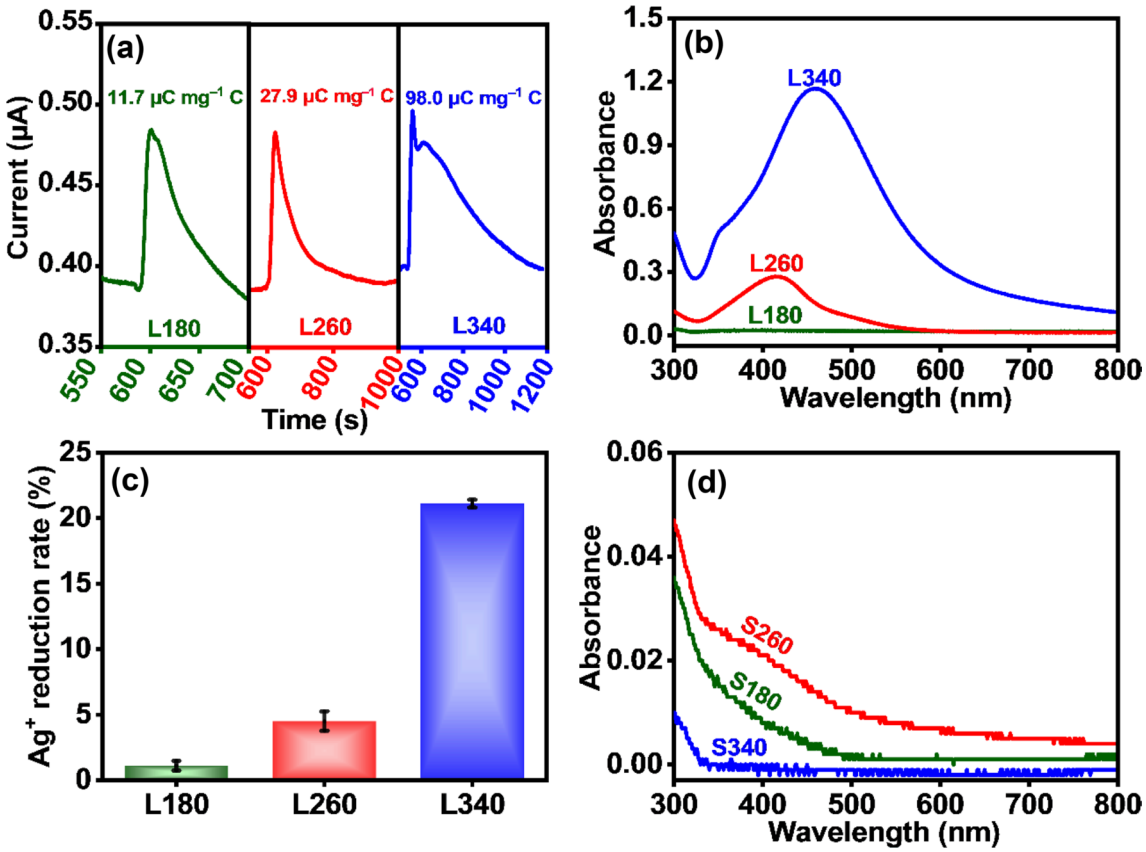

Fig. 2 Formation of silver nanoparticles in the presence of artificial humic substances and hydrochar under simulated sunlight. **a** Electron-donating capacities (EDC) of dissolved artificial humic substances prepared at different hydrothermal temperatures. **b** UV–vis absorption spectra of AgNPs in the presence of various dissolved artificial humic substances. **c** Reduction ratios of Ag^+ in the presence of various dissolved artificial humic substances (DOC = 35.6 mg C L^{-1}, $[Ag^+] = 1 \times 10^{-3}$ mol L^{-1}). **d** UV–vis spectra of AgNPs formed in the presence of hydrochars prepared at different hydrothermal temperatures ([hydrochar] = 100 mg L^{-1}, $[Ag^+] = 1 \times 10^{-3}$ mol L^{-1})

nano-silver can be generated in the presence of artificial humic substances under simulated sunlight.

3.3 Mechanisms of photoreduction of Ag^+

Several associated parameters, including artificial humic substance concentrations, Ag^+ concentrations, and pH, were varied to elucidate the potential mechanism of Ag^+ photoreduction by L340. The surface plasmon resonance (SPR) peak of AgNPs was broader at lower concentrations of artificial humic substances or Ag^+ (Fig. 3a,b), indicating an insufficient amount of reactive species to reduce and stabilize AgNPs with small particle sizes (Adegboyega et al. 2013; Akaighe et al. 2011). The increase in the growth rate of AgNPs correlated positively with the rise in pH, which was substantiated by the amplified SPR peak intensity of AgNPs as the pH increased (Fig. 3c). In contrast to alkaline environments, the formation of AgNPs may not be favorable in acidic environments because AgNPs are prone to dissolution under acidic conditions (Huang et al. 2019; Peretyazhko et al. 2014).

The role of $O_2^{\bullet-}$ in the reduction of Ag^+ was verified by purging with gas or adding SOD. The presence of $O_2^{\bullet-}$ can be determined by applying the EPR technology and using 5,5-dimethyl-1-pyrroline-N-oxide (DMPO) as a spin trap (Wang et al. 2020). As illustrated in Fig. 3d, six characteristic peaks of the DMPO—$O_2^{\bullet-}$ spin adducts were observed in the L340 suspension under simulated sunlight. However, with prolonged irradiation time, the $O_2^{\bullet-}$ content attenuated severely and was not detectable after 2 h of irradiation (Fig. 3e). The role of $O_2^{\bullet-}$ in photoreduction was further elucidated by the presence of SOD (Fig. 3f), which stopped AgNP formation, confirming that $O_2^{\bullet-}$ is the key reductant in the artificial humic substances-induced photoreduction. However, the photoreduction formation rate of AgNPs increased significantly in the nitrogen-purged condition (Fig. 3g-i), indicating that $O_2^{\bullet-}$ is not the only reductant in the reduction of Ag^+. These results show that the LMCT is a

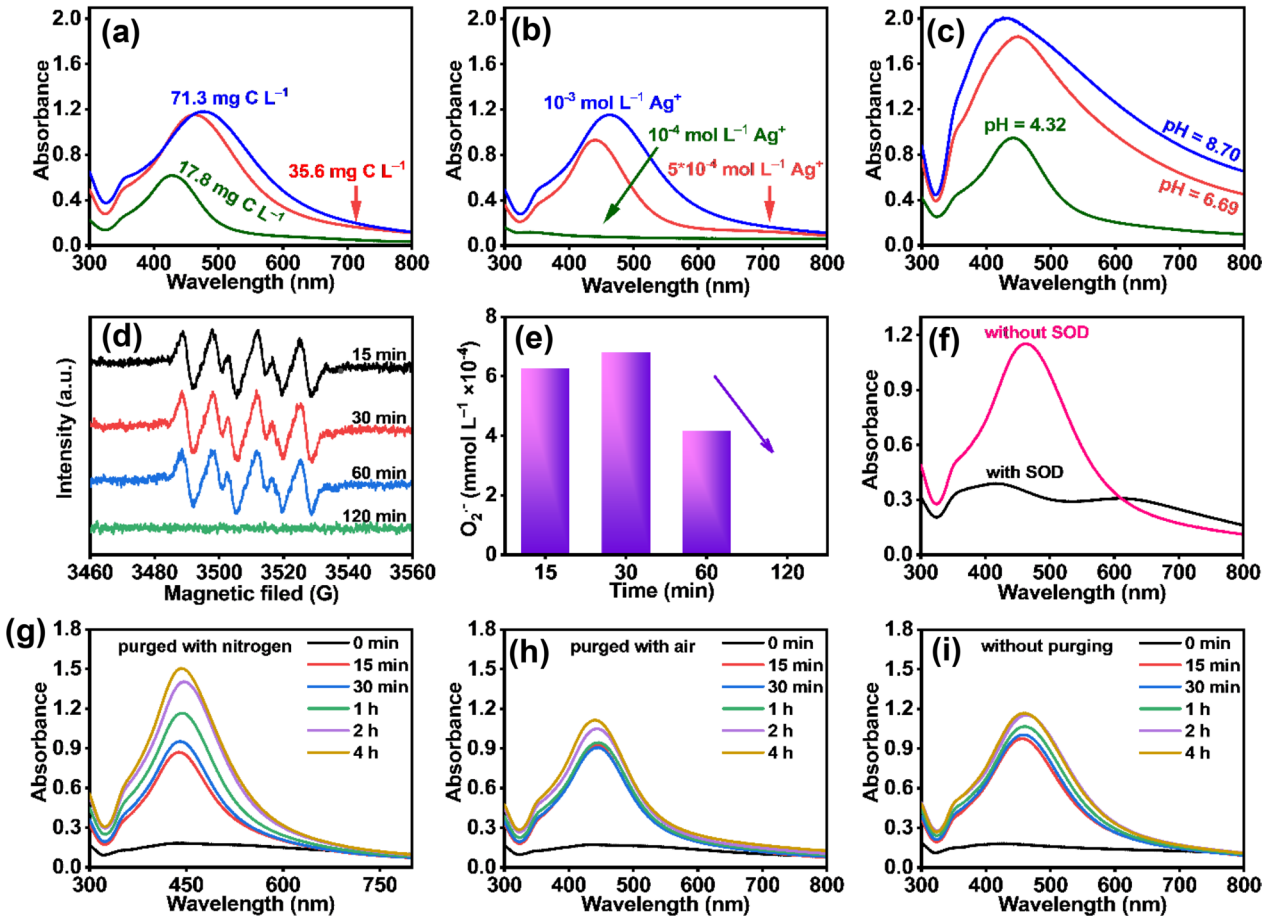

Fig. 3 Mechanisms of AgNP formation. **a** Effects of different concentrations of < 50 kDa M_f-L340 (17.8–71.3 mg C L^{-1}). **b** Effects of different Ag^+ concentrations (10^{-4}–10^{-3} mol L^{-1}). **c** Effects of different initial pH values (4.32–8.70). **d** EPR spectrum of the DMPO adduct with $O_2^{\bullet-}$ in the presence of artificial humic substances under simulated sunlight. **e** Quantification of $O_2^{\bullet-}$. **f** UV–vis absorption spectra of AgNPs with and without 3000 U mL^{-1} SOD under simulated sunlight. **g** UV–vis absorption spectra of AgNPs in L340 suspensions with nitrogen purging under simulated sunlight. **h** UV–vis absorption spectra of AgNPs in L340 suspensions with air purging under simulated sunlight. **i** UV–vis absorption spectra of AgNPs in L340 suspensions without purging under simulated sunlight (DOC = 35.6 mg C L^{-1}, $[Ag^+] = 1 \times 10^{-3}$ mol L^{-1})

pathway for the photoreduction of Ag^+, and jointly with $O_2^{\bullet-}$, is responsible for the artificial humic substances-induced photoreduction of Ag^+.

The photoreduction of Ag^+ to AgNPs was explored using 1 mmol L^{-1} $AgNO_3$ and 35.6 mg L^{-1} DOC of pristine or M_f-L340 under simulated sunlight. The SPR peak intensities of AgNPs in pristine and < 50 kDa M_f-L340 increased with prolonged irradiation time (Fig. 4a,b), whereas no obvious SPR peaks were observed for AgNPs in the UV–vis spectra of < 5 kDa M_f-L340 and < 1 kDa M_f-L340 (Fig. 4c,d). This result indicated that the formation rate of AgNPs in the pristine and < 50 kDa M_f-L340 was much higher than that in the lower- MW M_f-L340. The SPR peak intensity of AgNPs in lower-MW M_f-L340 samples remained unchanged even if the irradiation time was prolonged, implying that the Ag^+ reduction ability of lower-MW M_f-L340 was weak under sunlight irradiation. However, the particle size of AgNPs was independent of the MW of dissolved artificial humic substances (Fig. S17), which was inconsistent with the UV – vis results. As previously reported, the light attenuation phenomenon of M_f-NOM may hide its real reductive ability (Yin et al. 2014). Given the crucial role of phenolic moieties in reducing Ag^+, we assessed the total phenolic content of artificial humic substances with varying MW. The total phenolic concentration in pristine or M_f-L340 followed the order pristine L340 ≈ 50 kDa M_f-L340 > 5 kDa M_f-L340 > 1 kDa M_f-L340 (Fig. 4e), and the EEM results further confirmed this order (Fig. S18). The phenolic moieties were the main contributors to the reduction capacity, as confirmed by the electrochemical test results (Fig. 4f and Fig. S19).

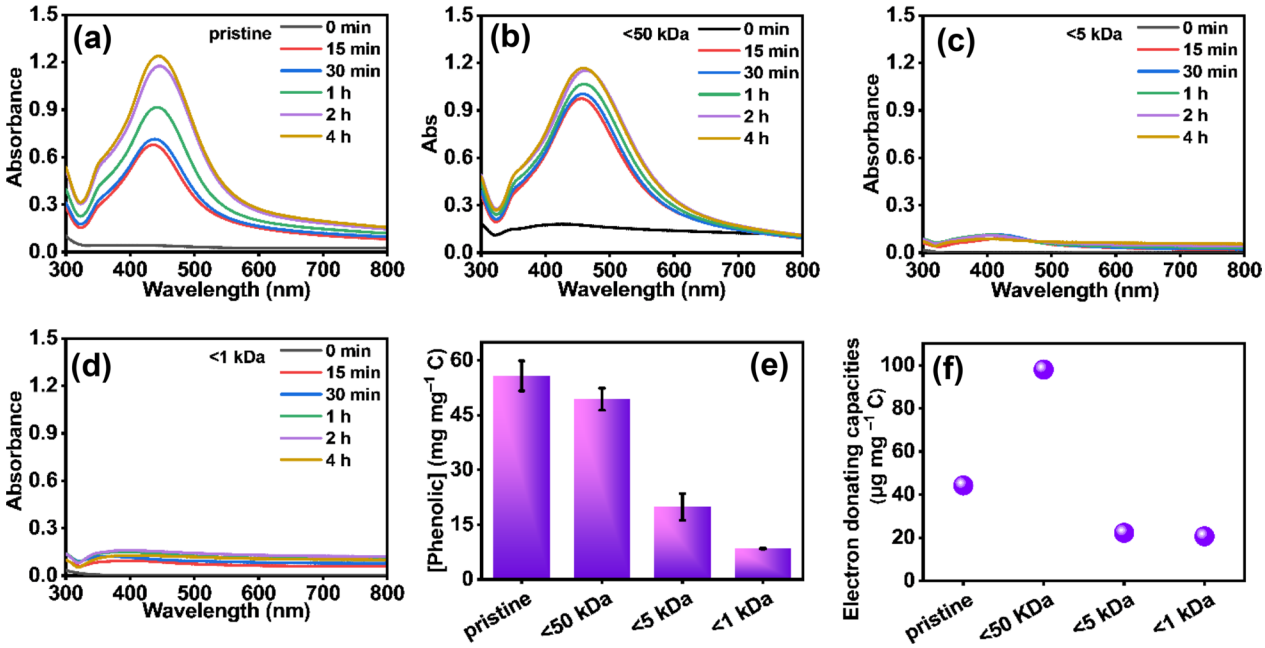

Fig. 4 Formation of silver nanoparticles in the presence of pristine L340 or M_f-L340 under simulated sunlight. **a** UV–vis absorption spectra of AgNPs formed with pristine L340. **b** UV–vis absorption spectra of AgNPs formed with < 50 kDa M_f-L340. **c** UV–vis absorption spectra of AgNPs formed with < 5 kDa M_f-L340. **d** UV–vis absorption spectra of AgNPs formed with < 1 kDa M_f-L340. **e** Total phenol content in dissolved artificial humic substances of different molecular weights. **f** EDC of dissolved artificial humic substances of different molecular weights (DOC = 35.6 mg C L^{-1}, $[Ag^+] = 1 \times 10^{-3}$ mol L^{-1})

3.4 Dissolution of hydrochar and promotes Ag^+ reduction

We further investigated the photoreduction potential of dissolved organic matter (DOM) derived from hydrochar upon prolonged sunlight exposure. Structural changes induced by sunlight irradiation significantly promoted hydrochar dissolution, evidenced by increased mass loss (Table S4) and decreased particle diameter (Fig. 5a). Additionally, an increase in the O/C atomic ratio confirmed progressive oxidation and enrichment of oxygen-rich functional groups (Fig. 5b).

GC–MS analysis revealed distinct compositional shifts in hydrochar-derived DOM following sunlight irradiation, showing enhanced formation of low-molecular-weight, oxygen-rich compounds over the irradiation periods (Fig. 5c). Correspondingly, TOC concentrations consistently increased, confirming continued DOM release (Fig. S20). The phenolic content gradually declined, indicating photochemical oxidation of phenolic moieties (Fig. S21). Moreover, DOM molecular weights exhibited a clear reduction, reflecting the progressive depolymerization into smaller molecules (Fig. S22). Meanwhile, an increased O/C ratio further suggested enhanced oxidation within DOM (Fig. S23).

With prolonged irradiation time, the SPR peak intensity increased significantly (Fig. 5c). The concentration of AgNPs increased from 11.0 mg L^{-1} after 15 min of irradiation to 25.9 mg L^{-1} for 4 h (Fig. S24). Remarkably, despite reduced phenolic content and molecular weights, DOM released from long-term irradiated hydrochar (S260) demonstrated significantly improved Ag^+ photoreduction performance (24% Ag^+ reduction ratio), representing a 5.3-fold enhancement compared to artificial humic substances synthesized at the same hydrothermal temperature (L260, Fig. 2c). This enhancement is likely attributable to increased superoxide radical generation and efficient LMCT mediated by newly formed oxygen-rich functional groups. These findings provide novel insights into the dynamic photochemical transformation pathways of hydrochar under natural sunlight exposure and their implications for environmental redox processes.

4 Conclusions

This study demonstrates that controlled hydrothermal humification (180–340 °C) of pine sawdust enables precise engineering of artificial humic substances with tunable phenolic architectures and electron-donating capacities. Using Ag^+ photoreduction as a model system, we show that 340 °C-derived artificial humic substances exhibit optimal performance (19.2-fold enhancement over 180 °C-derived samples) through $O_2^{\bullet-}$ generation by photoexcited phenolic groups. Crucially, we reveal the

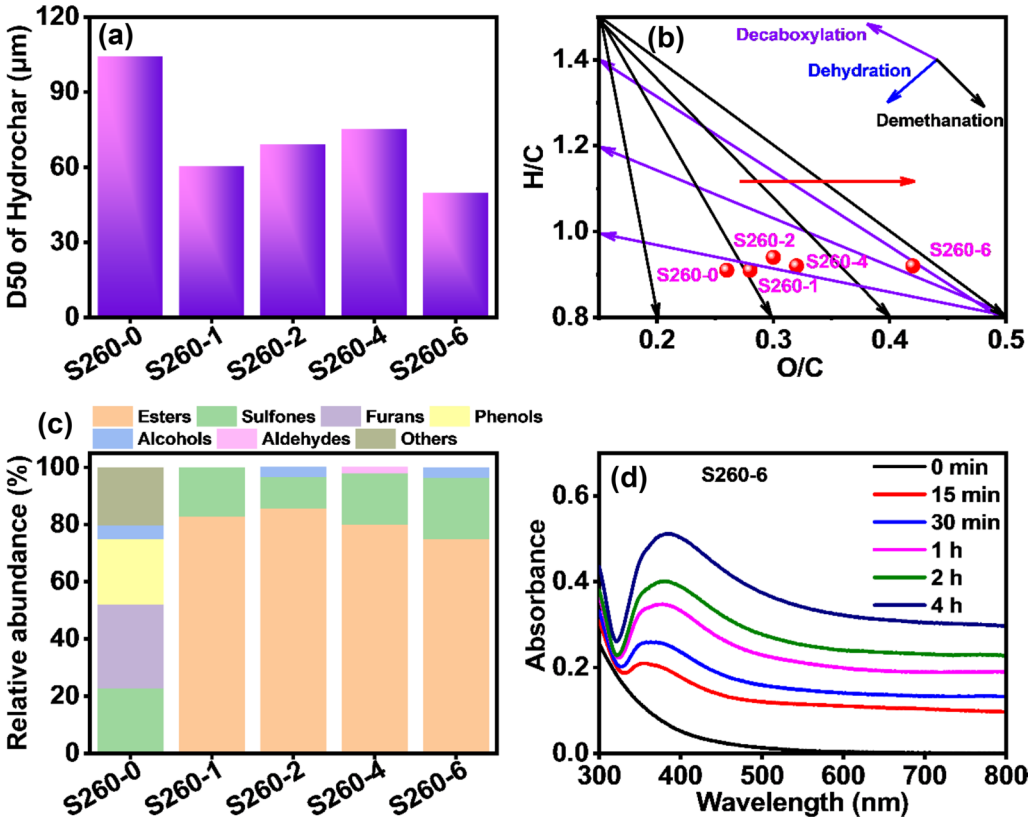

Fig. 5 Sunlight-induced hydrochar dissolution and enhanced Ag^+ reduction. **a** Particle size distribution (D50, median particle diameter) of S260 after simulated sunlight irradiation. **b** Evolution of H/C and O/C atomic ratios in the Van Krevelen diagram. **c** GC–MS analysis of DOM released from hydrochar after different irradiation times. **d** UV–vis spectra of AgNPs in the solution after irradiation of S260 (DOC = 35.6 mg C L^{-1}, $[Ag^+] = 1 \times 10^{-3}$ mol L^{-1})

novel phenomenon of sunlight-induced hydrochar dissolution, which dynamically enhances redox activity. These findings advance both: (1) the design of solar-responsive remediation materials through molecular-weight-controlled synthesis, and (2) the fundamental understanding of biochar's environmental transformations in sunlit systems.

Abbreviations

AgNPs	Silver nanoparticles
CRAM	Carboxylic-rich alicyclic molecule–like
DBC	Dissolved black carbon
DMPO	5,5-Dimethyl-1-pyrroline-N-oxide
DOM	Dissolved organic matter
EDC	Electron-donating capacities
EDS	Energy dispersive X-ray spectrometry
EEM	Excitation-emission matrix
FT-ICRMS	Fourier transformion cyclotron resonance mass spectrometry
GC–MS	Gas chromatography-mass spectrometry
HR-TEM	High-resolution transmission electron microscope
HTL	Hydrothermal liquefaction
ICP-OES	Inductively coupled plasma mass spectrometry
LMCT	Ligand-to-metal electron transfer process
MEO	Mediated electrochemical oxidation
M_f	Molecular weight fractionated
MW	Molecular weight
NOM	Natural organic matter
$O_2^{\bullet-}$	Superoxide radicals
SAED	Selected area electron diffraction
SOD	Superoxide dismutase
SPR	Surface plasmon resonance
TOC	Total organic carbon
XPS	X-ray photoelectron spectroscopy
XRD	X-ray diffraction

Supplementary Information

The online version contains supplementary material available at https://doi.org/10.1007/s42773-025-00526-3.

Additional file 1.

Author contributions

Liming Sun: Writing – review & editing, Writing – original draft, Formal analysis, Data curation, Methodology, Conceptualization. Minghao Shen: Formal analysis, Data curation. Chao Jia: Formal analysis, Data curation. Fengbo Yu: Formal analysis, Data curation. Shicheng Zhang: Writing – review & editing, Methodology, Conceptualization. Xiangdong Zhu: Writing – review & editing, Funding acquisition, Methodology, Conceptualization.

Funding

This work was supported by the National Natural Science Foundation of China (No. 22276040).

Availability of data and materials
The data proving the results of this study are available within the paper and related supplementary information.

Declarations

Competing interests
The authors have no competing interests to disclose.

Author details
[1]Department of Environmental Science and Engineering, Fudan University, Shanghai 200092, China. [2]State Key Laboratory of Soil and Sustainable Agriculture, Institute of Soil Science, Chinese Academy of Sciences, Nanjing 210018, China. [3]Shanghai Institute of Pollution Control and Ecological Security, Shanghai 200092, China.

Received: 26 December 2024 Revised: 9 September 2025 Accepted: 28 September 2025
Published online: 15 January 2026

References

Adegboyega NF, Sharma VK, Siskova K, Zboril R, Sohn M, Schultz BJ, Banerjee S (2013) Interactions of aqueous Ag^+ with fulvic acids: mechanisms of silver nanoparticle formation and investigation of stability. Environ Sci Technol 47:757–764. https://doi.org/10.1021/es302305f

Aeschbacher M, Sander M, Schwarzenbach RP (2010) Novel electrochemical approach to assess the redox properties of humic substances. Environ Sci Technol 44:87–93. https://doi.org/10.1021/es902627p

Akaighe N, Maccuspie RI, Navarro DA, Aga DS, Banerjee S, Sohn M, Sharma VK (2011) Humic acid-induced silver nanoparticle formation under environmentally relevant conditions. Environ Sci Technol 45:3895–3901. https://doi.org/10.1021/es103946g

Chen J, Fan X, Zhang L, Chen X, Sun S, Sun RC (2020) Research progress in lignin-based slow/controlled release fertilizer. Chemsuschem 13:4356–4366. https://doi.org/10.1002/cssc.202000455

Dong B, Liu G, Zhou J, Wang J, Jin R (2019) Transformation of silver ions to silver nanoparticles mediated by humic acid under dark conditions at ambient temperature. J Hazard Mater 383:121190. https://doi.org/10.1016/j.jhazmat.2019.121190

Dong B, Liu G, Zhou J, Wang J, Jin R, Zhang Y (2020) Effects of reduced graphene oxide on humic acid-mediated transformation and environmental risks of silver ions. J Hazard Mater. https://doi.org/10.1016/j.jhazmat.2019.121597

Guo X, Yin Y, Tan Z, Liu J (2018) Environmentally relevant freeze-thaw cycles enhance the redox-mediated morphological changes of silver nanoparticles. Environ Sci Technol 52:6928–6935. https://doi.org/10.1021/acs.est.8b00694

Hao S, Zhu X, Liu Y, Qian F, Fang Z, Shi Q, Zhang S, Chen J, Ren ZJ (2018) Production temperature effects on the structure of hydrochar-derived dissolved organic matter and associated toxicity. Environ Sci Technol 52:7486–7495. https://doi.org/10.1021/acs.est.7b04983

Hou WC, Stuart B, Howes R, Zepp RG (2013) Sunlight-driven reduction of silver ions by natural organic matter: formation and transformation of silver nanoparticles. Environ Sci Technol 47:7713–7721. https://doi.org/10.1021/es400802w

Huang Y-N, Qian T-T, Dang F, Yin Y-G, Li M, Zhou D-M (2019) Significant contribution of metastable particulate organic matter to natural formation of silver nanoparticles in soils. Nat Commun 10:3775. https://doi.org/10.1038/s41467-019-11643-6

Jain S, Mehata MS (2017) Medicinal plant leaf extract and pure flavonoid mediated green synthesis of silver nanoparticles and their enhanced antibacterial property. Sci Rep 7:15867. https://doi.org/10.1038/s41598-017-15724-8

Khan Z, Yang X-J, Fu Y, Joseph S, Khan MN, Khan MA, Alam I, Shen H (2023) Engineered biochar improves nitrogen use efficiency via stabilizing soil water-stable macroaggregates and enhancing nitrogen transformation. Biochar 5:52. https://doi.org/10.1007/s42773-023-00252-8

Liu H, Ge Q, Xu F, Qu X, Fu H, Sun J (2021) Dissolved black carbon induces fast photo-reduction of silver ions under simulated sunlight. Sci Total Environ 775:145897. https://doi.org/10.1016/j.scitotenv.2021.145897

Li L, Wang X, Fu H, Qu X, Chen J, Tao S, Zhu D (2020) Dissolved black carbon facilitates photoreduction of Hg(II) to Hg(0) and reduces mercury uptake by lettuce (Lactuca sativa L.). Environ Sci Technol 54:11137-11145. https://doi.org/10.1021/acs.est.0c01132

Li M, Dang F, Fu Q-L, Zhou D-M, Yin B (2018) Effects of molecular weight-fractionated natural organic matter on the phytoavailability of silver nanoparticles. Environ Sci Nano 5:969–979. https://doi.org/10.1039/c7en01173c

Lv J, Han R, Huang Z, Luo L, Cao D, Zhang S (2018) Relationship between molecular components and reducing capacities of humic substances. ACS Earth Space Chem 2:330–339. https://doi.org/10.1021/acsearthspacechem.7b00155

Nie X, Zhu K, Zhao S, Dai Y, Tian H, Sharma VK, Jia H (2019) Interaction of Ag^+ with soil organic matter: elucidating the formation of silver nanoparticles. Chemosphere 243:125413. https://doi.org/10.1016/j.chemosphere.2019.125413

Okolie JA, Nanda S, Dalai AK, Kozinski JA (2021) Optimization studies for hydrothermal gasification of partially burnt wood from forest fires for hydrogen-rich syngas production using Taguchi experimental design. Environ Pollut 283:117040. https://doi.org/10.1016/j.envpol.2021.117040

Peng X-X, Gai S, Cheng K, Yang F (2022) Roles of humic substances redox activity on environmental remediation. J Hazard Mater 435:129070

Peretyazhko TS, Zhang Q, Colvin VL (2014) Size-controlled dissolution of silver nanoparticles at neutral and acidic pH conditions: kinetics and size changes. Environ Sci Technol 48:11954–11961. https://doi.org/10.1021/es5023202

Qian F, Zhu X, Liu Y, Shi Q, Wu L, Zhang S, Chen J, Ren ZJ (2018) Influences of temperature and metal on subcritical hydrothermal liquefaction of hyperaccumulator: implications for the recycling of hazardous hyperaccumulators. Environ Sci Technol 52:2225–2234. https://doi.org/10.1021/acs.est.7b03756

Rtimi S, Dionysiou DD, Pillai SC, Kiwi J (2019) Advances in catalytic/photocatalytic bacterial inactivation by nano Ag and Cu coated surfaces and medical devices. Appl Catal B Environ 240:291–318. https://doi.org/10.1016/j.apcatb.2018.07.025

Tang C, Li Y, Song J, Antonietti M, Yang F (2021) Artificial humic substances improve microbial activity for binding CO_2. iScience 24:102647. https://doi.org/10.1016/j.isci.2021.102647

Walpen N, Getzinger GJ, Schroth MH, Sander M (2018) Electron-donating phenolic and electron-accepting quinone moieties in peat dissolved organic matter: quantities and redox transformations in the context of peat biogeochemistry. Environ Sci Technol 52:5236–5245. https://doi.org/10.1021/acs.est.8b00594

Wang BN, Liu HF, Zheng JB, Fan MT, Cao W (2011) Distribution of phenolic acids in different tissues of jujube and their antioxidant activity. J Agric Food Chem 59:1288–1292. https://doi.org/10.1021/jf103982q

Wang L, Lan X, Peng W, Wang Z (2020) Uncertainty and misinterpretation over identification, quantification and transformation of reactive species generated in catalytic oxidation processes: a review. J Hazard Mater 408:124436. https://doi.org/10.1016/j.jhazmat.2020.124436

Wang Y, Gu X, Huang Y, Ding Z, Chen Y, Hu X (2022) Insight into biomass feedstock on formation of biochar-bound environmentally persistent free radicals under different pyrolysis temperatures. RSC Adv 12:19318–19326. https://doi.org/10.1039/d2ra03052g

Xu S, Zhan J, Li L, Zhu Y, Liu J, Guo X (2023) Total petroleum hydrocarbons and influencing factors in co-composting of rural sewage sludge and organic solid wastes. Environ Pollut 319:120911. https://doi.org/10.1016/j.envpol.2022.120911

Yameen MZ, Naqvi SR, Juchelková D, Khan MNA (2024) Harnessing the power of functionalized biochar: progress, challenges, and future perspectives in energy, water treatment, and environmental sustainability. Biochar 6:25. https://doi.org/10.1007/s42773-024-00316-3

Yang F, Zhang S, Cheng K, Antonietti M (2019) A hydrothermal process to turn waste biomass into artificial fulvic and humic acids for soil remediation. Sci Total Environ 686:1140–1151. https://doi.org/10.1016/j.scitotenv.2019.06.045

Yang F, Tang C, Antonietti M (2021) Natural and artificial humic substances to manage minerals, ions, water, and soil microorganisms. Chem Soc Rev 50:6221–6239. https://doi.org/10.1039/d0cs01363c

Yang P, Jiang T, Cao D, Sun T, Liu G, Guo Y, Liu Y, Yin Y, Cai Y, Jiang G (2023) Unraveling multiple pathways of electron donation from phenolic moieties in natural organic matter. Environ Sci Technol 57:16895–16905. https://doi.org/10.1021/acs.est.3c05377

Yin Y, Shen M, Zhou X, Yu S, Chao J, Liu J, Jiang G (2014) Photoreduction and stabilization capability of molecular weight fractionated natural organic matter in transformation of silver ion to metallic nanoparticle. Environ Sci Technol 48:9366–9373. https://doi.org/10.1021/es502025e

Yu S, Liu J, Yin Y, Shen M (2018) Interactions between engineered nanoparticles and dissolved organic matter: a review on mechanisms and environmental effects. J Environ Sci 63:198–217. https://doi.org/10.1016/j.jes.2017.06.021

Yu F, Zhao W, Qin T, Zhao W, Chen Y, Miao X, Lin L, Shang H, Sui G, Peng D, Yang Y, Zhu Y, Zhang S, Zhu X (2022) Biosafety of human environments can be supported by effective use of renewable biomass. Proc Natl Acad Sci U S A 119:e2106843119

Zingaretti D, Lombardi F, Baciocchi R (2018) Soluble organic substances extracted from compost as amendments for Fenton-like oxidation of contaminated sites. Sci Total Environ 619:1366–1374. https://doi.org/10.1016/j.scitotenv.2017.11.178

Zou X, Shi J, Zhang H (2015) Morphological evolution and reconstruction of silver nanoparticles in aquatic environments: the roles of natural organic matter and light irradiation. J Hazard Mater 292:61–69. https://doi.org/10.1016/j.jhazmat.2015.03.005